Automation in Construction 155 (2023) 105051

Contents lists available at ScienceDirect

Automation in Construction

journal homepage: www.elsevier.com/locate/autcon

A bio-inspired solution to alleviate anisotropy of 3D printed engineered cementitious composites (3DP-ECC): Knitting/tilting filaments

Wen Zhou [a], Wes McGee [b], H. Süleyman Gökçe [c], Victor C. Li [a,*]

[a] Department of Civil and Environmental Engineering, University of Michigan, Ann Arbor, MI 48109, USA
[b] Taubman College of Architecture and Urban Planning, University of Michigan, Ann Arbor, MI 48109, USA
[c] Department of Civil Engineering, Bayburt University, Bayburt 69010, Türkiye

ARTICLE INFO

Keywords:
3D printed engineered cementitious composites (3DP-ECC)
Anisotropy
Knitting
Flexural property
Interface

ABSTRACT

Widely reported anisotropy in 3D printed cementitious structures has been a primary concern to structural integrity, especially for fiber-reinforced cementitious material, e.g., engineered cementitious composites (ECC). To alleviate the anisotropy present in 3D printed ECC (3DP-ECC), two innovative printing patterns, "knitting" and "tilting" filaments, were proposed, mimicking the natural crossed-lamellar structure of conch shells. 3D spatial paths were designed to allocate tensile/flexural resistance to multiple directions and to create an interwoven interface system to strengthen the structure. Four-point bending tests loading from three different directions were conducted. It was found that knitted and tilted filaments revealed superior or comparable bending performance to cast ECC in two favorable orientations. Furthermore, flexural performance in the weakest orientation was notably improved by knitting and tilting, with up-to-179% increases in flexural strength compared with that of parallel filaments. This novel approach holds great promise in alleviating anisotropy of 3DP-ECC without introducing additional reinforcement.

1. Introduction

Extrusion-based 3D printing (3DP) of cementitious material transcends the traditional construction mode, showing distinct superiorities in enabling complex geometries, promoting construction efficiency, eliminating formwork, reducing labor, and minimizing the environmental impact of the construction industry [1–7]. The advent of 3D printing has opened up exciting prospects for application in various engineering domains. In recent years, this emerging technology has witnessed a proliferation of application cases (Fig. 1), demonstrating its vast potential in diverse fields such as house construction, bridge engineering, landscape decoration, etc. [8–10]

1.1. Anisotropy concern in 3D printing

As an advanced additive manufacturing technology, 3DP allows the automatic generation of a layered element. The layering process inevitably introduces interfaces into the 3DP structure and causes property deviation of the interlayer surface from the bulk material [17]. During the deposition and stacking of filaments, air voids could be entrapped between adjacent filaments and successive layers, undermining the interfacial properties [18]. Further, while the former layer of material undergoes rapid structuration after extrusion, it is gradually losing its ability to establish a tight bond with the next layer of wet material. Fast structuration, high thixotropy, long cycling time, and moisture loss at the surface may result in cold joints at the position of interfaces and threaten the integrity of the manufactured objects [19–25]. Consequently, anisotropic mechanical properties are inadvertently introduced into the laminated structure owing to the existence of interfaces between printed filaments and layers.

Anisotropy in 3D printed objects was widely reported - their directionally dependent mechanical properties vary significantly with the loading orientations [26–28]. In flexural, tensile, and compressive tests, loadings from the three different orientations in Fig. 2 yield different results. Generally, the flexural and tensile properties obtained from Orientation I are the most favorable. In contrast, Orientation III exhibits inferior bending and tensile performance. When tensile forces act directly on the interfacial planes, i.e., the weak link in the structure, crack propagation and ultimate failure tend to occur at the interface position before the bearing capacity of the bulk material is exhausted [29]. In terms of compressive strength, the effect of anisotropy seems less prevalent [30,31].

* Corresponding author.
E-mail addresses: wzhoucee@umich.edu (W. Zhou), wesmcgee@umich.edu (W. McGee), suleymangokce@bayburt.edu.tr (H.S. Gökçe), vcli@umich.edu (V.C. Li).

https://doi.org/10.1016/j.autcon.2023.105051
Received 28 November 2022; Received in revised form 11 June 2023; Accepted 3 August 2023
Available online 9 August 2023

For 3D printed fiber-reinforced cementitious material, the situation is further complicated. Fiber reinforcement is regarded as an effective means to promote the flexural and tensile performance of the printed components. Previous studies reported significant enhancement of flexural performance with various types of fibers, including polypropylene (PP) fiber [18,30,32], polyethylene (PE) fiber [33–35], polyvinyl alcohol (PVA) fiber [36,37], glass fiber [31], carbon fiber [38], basalt fiber [26,38] and steel fiber [39]. For example, 0.25 vol% PP fiber was reported to improve the flexural strength of 3D printed geopolymers by up to 34%, while 0.75 vol% and 1.0 vol% PP fibers could trigger flexure-hardening behavior [32]. Le et al. [18] observed an increase in flexural strength of up to 45% when a small amount of PP fibers was included.

With the addition of fibers and the extrusion process of 3DP, the tensile and flexural properties in the in-plane direction (Orientation I) are significantly improved due to more consistent fiber orientation [26,37,38], even surpassing the performance of the cast specimens. With 2.0 vol% PE fibers, a 14% increase was observed in the tensile strain capacity of 3D printed engineered cementitious composites (ECC) compared with cast ECC [33]. Yu et al. [40] and Xu et al. [41] also suggested higher tensile strengths and strain capacities of printed ECC. With aligned fibers reinforcing the matrix along the printing direction, anisotropy is expected even within a single filament and exaggerated in the whole picture of the printed structure.

Intuitively, specimen loaded in Orientation III shows inferior flexural and tensile performance compared with the other two directions, as the resistance capacity in Orientation III highly depends on the interlayer bonding characteristics. In addition to the aforementioned factors, the lack of fiber bridging at the interface is another primary concern in fiber-reinforced cementitious material [34]. Previous studies showed up-to-74% drops in flexural strength of printed fiber-reinforced cementitious material when switching the loading orientation from Orientation I to Orientation III [29,30,42]. Regarding Orientation II, the flexural performance is usually between those in the other two directions [26]. Some test results on the mechanical properties of 3DP synthetic fiber-reinforced cementitious materials in previous literature are summarized in Tables 1a and 1b.

The anisotropy characteristic renders different material behaviors of printed elements from those of cast concrete and challenges the structural performance. Various methods have been proposed to meet the anisotropic challenge. One attempt is to apply adhesive agents to the interface. Cement paste [43], sulfur and black carbon-based polymers [44], and cellulose fiber-reinforced cement [45], for example, are used as adhesive agents to be brushed on the surface of the newly printed layer. However, this method either requires additional human labor and thus negates the automation of the entire manufacturing process or demands extra preparation and extrusion of the agents, undermining the efficiency of manufacturing. Another technique is to enhance interfacial bonding through mechanical interlock, for instance, by integrating the tongue and groove technology into 3D printing to obtain a grooved geometry [19,46] or modifying the layer surface to make it rough enough to adhere to the next layer [47]. In addition, inserting reinforcements in the vertical direction is also a popular strategy. Steel wire mesh [48], straight steel bar or fiber [49,50], and staple/U-nail [51,52] have been embedded perpendicular to the printing plane to provide interlayer reinforcements. These beneficial attempts offer a means of enhancing the mechanical performance in Orientation III with external reinforcements. Nonetheless, for fiber-reinforced cementitious ink, e.g., ECC, it may be more concise and effective to utilize the inherent internal reinforcement and directional-dependent features to alleviate the anisotropy.

1.2. Bio-inspired approach

Taking advantage of 3DP's feature of enabling complex paths and the orientation-dependent properties of fiber-reinforced composites, anisotropy could be alleviated without introducing any external reinforcements. As elucidated before, the tensile and flexural behavior of 3DP fiber-reinforced materials is most favorable in one direction (commonly the direction of filament generation). Through the delicate design of 3D spatial paths, filaments are deposited in different orientations, thus allocating tensile/flexural resistance capacity to multiple directions. In addition, 3D spatial path design alters the simple and unitary orientation of interfaces yielded by traditional in-plane printing (despite various infilling patterns and toolpaths in a single plane [53]), complicating the weakest path along which cracks propagate along, thereby delaying the occurrence of failure.

The design of the 3D spatial patterns is inspired by the natural crossed-lamellar structure of conch shells. As shown in Fig. 3, conch shell possesses macroscopic layers which are composed of three orders

Fig. 1. 3D printed showcases: (a) Wujiazhuang farmhouse, China [11]; (b) Nijmegen bicycle bridge, Netherlands [12,13]; (c) Striatus bridge, Italy [14,15]; (d) Shell pavilion [16].

of lamellas. Within each macroscopic layer, multiple layers of first-order lamellae are arranged perpendicular to the macroscopic layers and inclined relative to one another. These first-order lamellae contain parallel stacks of long, thin laths, referred to as second-order lamellae, which are further composed of single crystal third-order lamellae. The interwoven interfaces created by the laminate structures in multiple orientations empower the conch shell with high ductility in bending tests despite the brittle nature of its compositions (99 vol% of aragonite, a polymorph of calcium carbonate). Upon loading, multiple channel cracks developed along first-order interfaces can be arrested by the tough middle layer. Catastrophic failure is therefore mitigated. The fracture toughness of conch shells exceeds that of single crystals of the pure mineral by two to three orders of magnitude [54,55]. Mimicking this biological nature, bio-inspired printing patterns were designed, aiming at higher flexural strength and ductility of the printed structures.

In this study, the focus is specifically placed on the 3D printing of engineered cementitious composites (3DP-ECC). As a promising printing ink, ECC exhibits robust tensile ductility and strain-hardening behavior, especially in Orientation I [33,35,36,40,46,56–58]. To endow 3DP-ECC with appropriate spatial orientations, knitted and tilted structures were designed and printed. Flexural tests from various orientations were conducted to probe the anisotropic characteristics of these innovative structures.

2. Experimental programs

2.1. Materials

The binders used to prepare printable ECC includes ordinary Portland cement (Type IL, Lafarge-Holcim) and fly ash (Class F, Boral Resources), the chemical compositions of which are listed in Table 2 [56]. Fly ash was employed to enhance the flowability/extrudability and reduce the carbon footprint of the ECC mixture. Silica sand (F75, US Silica) was adopted as fine aggregate. PVA fibers with a length of 8 mm, which demonstrate sufficient ease in printing and yield remarkable mechanical performance, were employed as reinforcement of ECC. The properties of the micro PVA fibers are listed in Table 3.

The mix proportions of printable PVA-ECC are shown in Table 4. The water-to-binder ratio and sand-to-binder ratio are 0.25 and 0.26, respectively. The dosage of PVA fiber is 2.0% by volume of the total composition. The bulk density of the material is 1959 kg/m^3. Tensile properties of cast PVA-ECC at the age of 28 days are shown in Fig. 4. For 3D printing, the fresh mixture of PVA-ECC was transferred directly from the mixer to the material hopper 20 min after water addition.

2.2. Printing setup

The 3D printing system shown in Fig. 5 consists of three main parts. Fresh ECC material is fed into the hopper, which is connected to a peristaltic pump system, and then transported through a 15 ft. hose to the printing tool. At the inlet position of the printing tool, a pressure sensor is mounted to detect the pressure fluctuation of material flow and feed the signal back to the peristaltic pump to realize real-time monitoring and adjustment of the pressure. After pumped into the printing tool, fresh material is extruded from a nozzle by a built-in progressive cavity pump inside the tool. A 6-axis KUKA robot fulfills the precise positioning and controlling of the printing head.

2.3. Printing patterns

2.3.1. Parallel filaments

Parallel filaments are the most common pattern of 3D printed structures in practice. Parallel filaments are usually deposited in a fixed sequence layer by layer, as shown in Fig. 6a. Each layer is deposited on the printing plane (x-y plane), and then the printing tool advances to the next layer, building up structure height in the vertical direction (z-axis). A Rhino model of parallel filaments path adopted in this research is shown in Fig. 6b. The fillets at the end of filaments are designed to avoid sharp corners and help the tool align smoothly.

This printing pattern is valued for being straightforward to design and requires only three degrees of freedom for a 3D printer. However, the presence of anisotropy is a primary concern for parallel filaments. As printing is restricted in the x-y plane, layer interfaces along the z-direction are prone to insufficient bonding and potential cold joints. This issue requires particular attention for fiber-reinforced cementitious materials, e.g., ECC. Due to fiber alignment along the printing direction (x-axis) led by extrusion, fibers' effect of bridging cracks in the x-y plane and in the z-direction shows a dramatic discrepancy. Four-point bending tests were conducted in three different loading scenarios (Fig. 6c) to quantify the anisotropy of parallel ECC filaments. The test setup is detailed in Subsection 2.4.

2.3.2. Knitted filaments

Knitting filaments describes a printing pattern mimicking the crossed-lamellar micro-structure of conch shells. The printing process for this pattern is schematically depicted in Fig. 7a. For step ①, two parallel filaments are deposited along the x-axis on the printing base, and another single filament is placed on top of the first layer. Following this, in step ②, stair-wise filaments are generated back and forth in the y-z plane until the previous filaments are fully covered. Then another "layer" of parallel filament is extruded, as in step ③, on the upper surface of the "stair steps". Parallel filaments and stair-wise filaments are

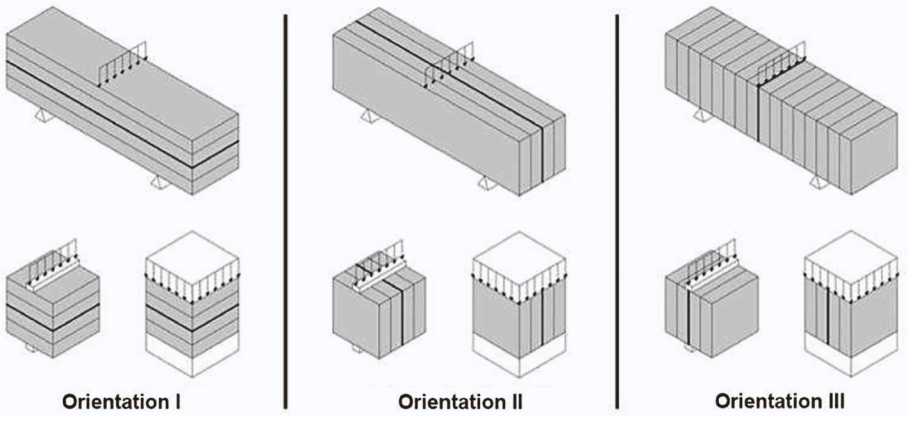

Fig. 2. Directionally dependent mechanical tests respective to layer orientation (adapted from [30]).

Table 1a
Studies on anisotropic properties of 3D printed cementitious materials.

Authors	Binders	Aggregates	Admixtures	w/b	Fiber type	Fiber length (mm)	Fiber content	Orientation	Flexural strength (MPa)	Tensile strength (MPa)	Tensile strain capacity (%)	Compressive strength (MPa)
Le et al. (2012) [18]	OPC, FA, SF	silica sand	SP, retarder, accelerator	0.26	PP	12	1.2 kg/m^3	I	12–17 (11)			84–102 (107)
								II	13 (11)			77–95 (107)
Nematollahi et al. (2018) [59]	FA	silica sand	CMC	0.38	PP	6	0.75 vol %	I	6.1			25.9
								II	6.5			13
								III				17.7
							1.0 vol %	I	7.5			18.2
								II	7.5			15.4
								III				14.5
Wolfs et al. (2019) [30]	OPC, LP	silica sand	rheology modifiers	0.495	PP		Little	I	4.29 (4.28)	3.68 (4.11) (SP)		28.51 (42.3)
								II	4.7 (4.28)	3.72 (4.11) (SP)		29.19 (42.3)
								III	3.68 (4.28)	3.55 (4.11) (SP)		29.19 (42.3)
Figueiredo et al. (2020) [37]	OPC, BFS, LP	–	SP, VMA	0.20	PVA	8	2.0 vol %	I	7.2–7.5	2.4	0.26	44.09
								II		2.41	0.31	41.93
	OPC, FA, LP	silica sand	SP, VMA	0.28				I	3.4–3.9	1.64	0.15	17.66
								II		1.65	0.24	15.02
Ding et al. (2020) [34]	OPC	silica sand	SP, HPMC	0.35	PE	6&12	1.0 wt% (in total)	I	9.53 (10.05)			
								II	8.88 (10.05)			
							1.4 wt% (in total)	I	10.29 (15.09)			
								II	11.54 (15.09)			
Yu et al. (2021) [40]	OPC, FA	silica sand	SP, HPMC	0.24	PVA	8	2.0 vol %	I		3.38 (3.36)	3.09 (3.00)	28–31 (31.2)
								III				21–24 (31.2)

Table 1b
Studies on mechanical properties of 3D printed cementitious materials.

Authors	Binders	Aggregates	Admixtures	w/b	Fiber type	Fiber length (mm)	Fiber content	Orientation	Flexural strength (MPa)	Tensile strength (MPa)	Tensile strain capacity (%)	Compressive strength (MPa)
Zhu et al. (2021) [61]	OPC, FA, SF, SAC	silica sand	SP, HPMC	0.26	PE	6&12	2.0 vol% (in total)	I	6.28 (4.95)			
								II	4.83 (4.95)			
Ye et al. (2021) [62]	OPC, FA, SF	silica sand	SP	0.26	PE	18	2.0 vol%	I	14.5 (15.1)	4.67 (6.81)	7.50 (9.81)	45.8 (38.8)
								II	14.4 (15.1)			40.4 (38.8)
								III				40.2 (38.8)
Ding et al. (2021) [63]	OPC	silica sand	SP, HPMC	0.35	PE	6&12	1.4 wt% (in total)	I	12.3 (13.9)			
								II	13.6 (13.9)			
Aslani et al. (2022) [64]	OPC, FA, SF	silica sand, crumb rubber	SP	0.27	PVA	12	1.75 vol % of binder	I	9.2 (3.5)			33.5 (32.5)
								III				34.5 (32.5)
Sun et al. (2022) [42]	SAC, SF, mineral powder	silica sand	SP, retarder	0.16	PVA	9	1.2 vol%	I	13.9 (13.0)			75 (81)
								II	13.5 (13.0)			70 (81)
								III	8.3 (13.0)			66 (81)

Note: Figures inside the parenthesis are the corresponding data of the mold-cast specimens; SP inside the parenthesis: splitting tensile strength; OPC: ordinary Portland cement; FA: fly ash; SF: silica fume; SAC: sulfoaluminate cement; LP: limestone powder; SP: superplasticizer; VMA: viscosity modifying agent; HPMC: hydroxypropyl methylcellulose; NC: nanoclay; CMC: sodium carboxymethyl cellulose; PP: polypropylene; PE: polyethylene; PVA: polyvinyl alcohol; HDPE: high-density polyethylene.

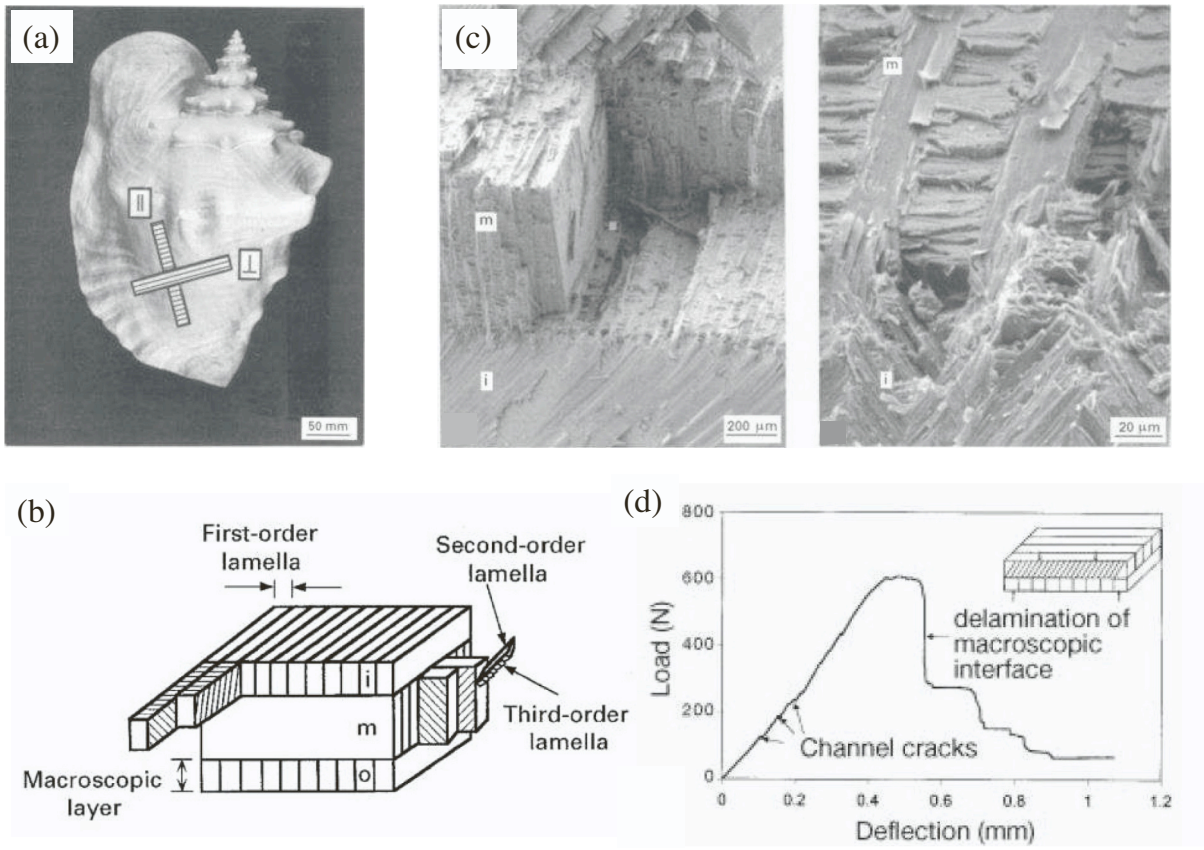

Fig. 3. (a) A *strombus gigas* conch shell, (b) the schematic drawing of its crossed-lamellar structure, (c) the fracture surfaces under four-point bending, and (d) the load-deflection curve under four-point bending. ((a-c) were adapted from [54]; (d) was adapted from [55]).

Table 2
Chemical compositions of OPC and FA (wt%).

Material	CaO	Al_2O_3	SiO_2	SO_3	Fe_2O_3	MgO	Others
OPC	63.5	4.8	19.6	2.6	2.9	2.2	4.4
FA	17.4	19.8	39.4	1.9	11	3.7	6.8

Note: OPC: ordinary Portland cement; FA: fly ash.

deposited alternatively on top of each other, creating an interwoven 3D pattern of ECC filaments. A Rhino printing path design corresponding to knitting pattern is presented in Fig. 7b. Fig. 7c shows four-point bending tests in three different loading orientations.

Compared with the traditional parallel pattern, the most prominent features of knitting design are:

(1) Knitting transcends the regular practice of single-layer printing in the two-dimensional plane (x-y plane) and unidirectional stacking in the third dimension. It expands both the single filament path and the overall structure construction to an actual three-dimensional space. This three-dimensional space design renders the direction-dependent mechanical properties of ECC (excellent tensile ductility in the printing direction) to the element out of the conventional printing plane (x-y plane). It is an attempt to homogenize material performance at the structural level through architectural design.

(2) Compared with parallel filaments, the knitting process introduces a more complex three-dimensional interface system, which converts interface from the original weakness into a structural strengthening method. The interface is generally considered relatively brittle. Even with highly ductile ECC materials printed, the interface can produce a brittle or quasi-brittle mechanical response due to the lack of fiber connections. However, the complex staggered interfaces in the conch shells enable brittle materials to yield excellent fracture toughness by forcing the crack front to twist as it propagates. Similarly, in the structural design of 3DP-ECC, intentionally creating tortuous and rugged interfaces could induce the development of multiple cracks, promotes energy dissipation, and delays crack penetration.

2.3.3. *Tilted filaments*

Alternating deposition of cross-ply structure (0° and 90° filaments, sometimes also including 45° filaments) is a common practice to moderate the in-plane anisotropy of 3DP. However, this design generally

Table 4
Mix proportions of printable PVA-ECC (Unit: kg/m^3).

OPC	FA	Sand	Water	SP	PVA Fiber
497	781	332	320	2.5	26

Note: SP: superplasticizer.

Table 3
Properties of PVA fiber.

Length (mm)	Fiber diameter (μm)	Young's modulus (GPa)	Density (kg/m^3)	Surface oil content (wt%)	Elongation (%)	Nominal Strength (MPa)
8	39	42.8	1300	1.2	6.0	1600

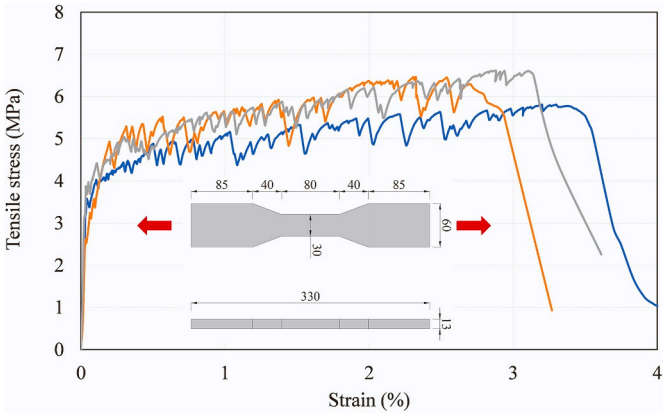

Fig. 4. Tensile properties of cast ECC under direct tensile tests. (The unit of specimen geometries is mm. Curves shown in the figure represent three identical specimens in the same group.)

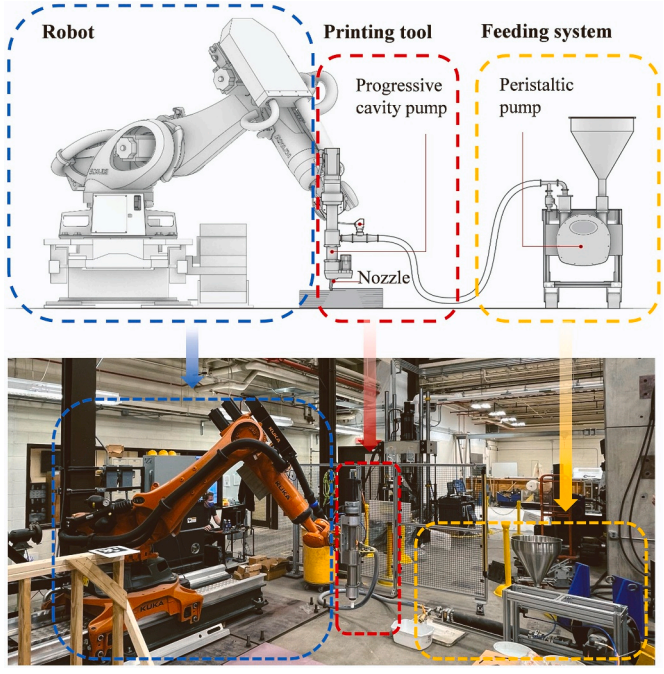

Fig. 5. Printing setups.

does not contribute to performance improvement in the vertical direction (z-axis). Therefore, a tilted pattern was proposed. Filaments at 0° (along the x-axis) and 90° (along the y-axis) are alternatively deposited in layers; nevertheless, instead of printing on the conventional x-y plane, the deposition occurs on the top surface of an inclined base, which was printed first at an angle to the x-y plane, as shown in Fig. 8a. The base is shaped by stacking several layers of filaments along the x-axis to form an inclined surface (step ①). A layer of parallel filaments is then placed along the x-direction with the same inclination as the base (step ②), followed by a next layer of parallel filaments along the y-z plane (step ③). Repeat steps ② and ③ until the desired dimension and shape are achieved. A Rhino model for tilted pattern and three different loading orientations are illustrated in Fig. 8b and Fig. 8c, respectively. The printed structures in this research were tilted by 27°.

The underlying logic of tilting design is analogous to that of knitting: to endow the printed structure with tensile/bending resistance in the y- and z-directions, and to bring in a more advanced interface system. By simply tilting a basic printing pattern at an angle, the interfaces are

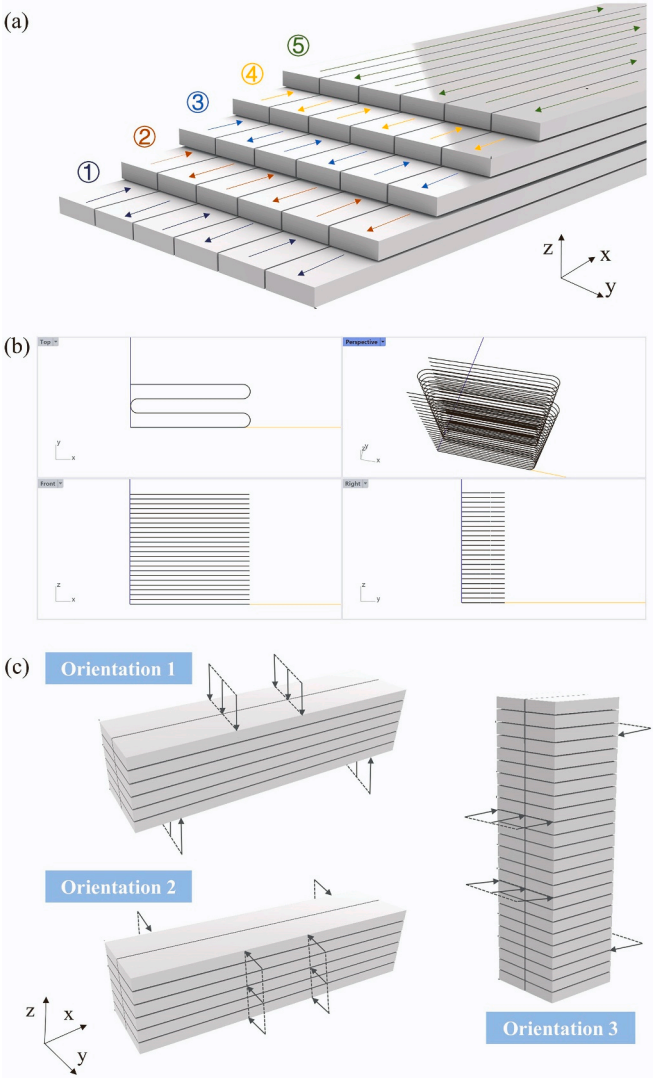

Fig. 6. (a) Schematic diagram, (b) Rhino model, and (c) different loading scenarios for parallel filaments. (Interfaces are exaggerated in the schematic diagrams to show the positions.)

elongated in length and could contribute to delay fracture, although it does not produce zig-zag interfaces as in knitting.

2.4. Four-point bending tests

To prepare specimens for four-point bending tests, the printed objects were cut into smaller beam specimens by saw. As the bending tests were conducted in different loading orientations, two types of specimens, i.e., with the longest side along the x-direction and z-direction, were manufactured. The sampling process avoided the uneven surface area of printed elements in case unexpected defects near the surface affect the consistency in mechanical performance. The geometries of the specimens were 200 mm in length, 50 mm in width, and 50 mm in depth.

The test system (Fig. 9a) consists of three main parts: (1) loading setup, (2) motion capture system, and (3) digital image correlation (DIC) system. The four-point bending tests were carried out on an MTS 810 machine, as shown in Fig. 9b. The three loading spans were 50 mm, 60 mm, and 50 mm, respectively (Fig. 9c). The loading rate was 0.2 mm/min. Four kinematic markers were attached to the specimen to locate the position of specific points on the surface. The absolute position changes of the markers were captured by an NDI Optotrak motion capture system shown in Fig. 9d to derive the mid-span deflection of the specimen. In

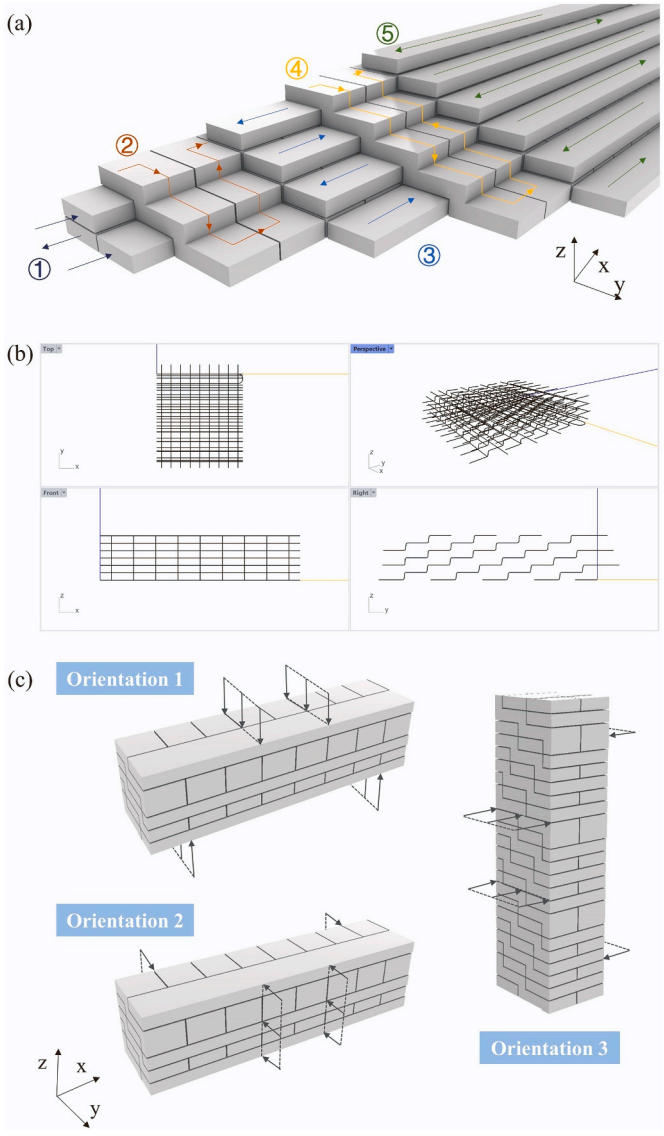

Fig. 7. (a) Schematic diagram, (b) Rhino model, and (c) different loading scenarios for knitted filaments. (Interfaces are exaggerated in the schematic diagrams to show the positions.)

addition, a high-resolution camera and a lighting system were placed in front of the specimen, to monitor the morphological and positional changes of the random black and white speckles on the specimen surface for DIC analysis.

3. Results and discussions

3.1. Flexural properties of parallel filaments

Fig. 10a illustrates the four-point bending test results for parallel filaments and cast ECC specimens. The relationships between flexural stress and mid-span deflection are shown. The flexural stress was calculated according to Eq. (1), and the mid-span deflection was derived from the relative position change of the four markers shown in Fig. 9b.

$$\sigma = \frac{3F(L - L_i)}{2bd^2} \tag{1}$$

where F is the load; L is the length of the support span, i.e., 160 mm in this research; L_i is the inner span, i.e., 60 mm; b and d are the width and depth of the specimen, respectively.

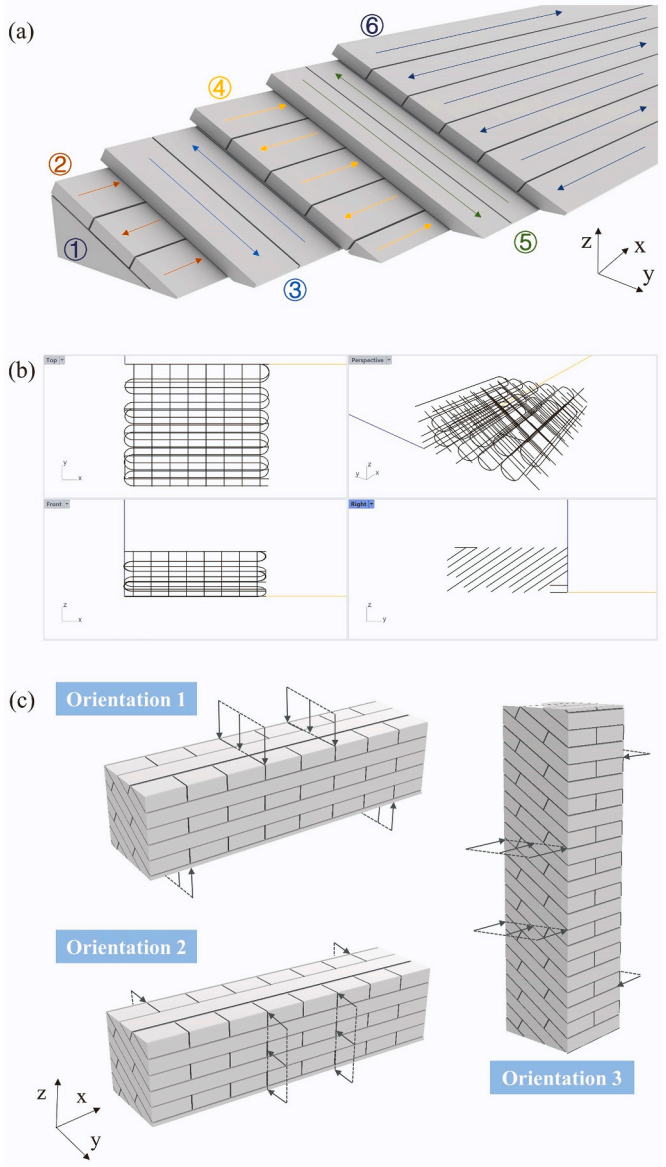

Fig. 8. (a) Schematic diagram, (b) Rhino model, and (c) different loading scenarios for tilted filaments. (Interfaces are exaggerated in the schematic diagrams to show the positions.)

Parallel filaments loaded in Orientation 1 (abbreviated as PA1) showed excellent flexural performance in both flexural strength and mid-span deflection. The PA1 group exhibited unparalleled flexural resistance, with an average flexural strength exceeding 21 MPa. Robust strain-hardening behavior was observed. The fluctuation of load originated from the successive development of multiple micro-cracks. As each new micro-crack developed, the brittle cementitious matrix was unable to bear the stress, resulting in a slight stress drop. Nonetheless, as the stress redistributed between fibers and matrix, the load-bearing capacity of the specimen was elevated to a higher level than the original stress peak. The strain hardening continued until stress concentration occurred on one crack plane with the lowest load capacity, causing the crack opening to gradually grow until fracture. This process is analogous to the plastic yielding in ductile metal and empowers ECC with the unique "metallic" tensile ductility [58].

The failure mode of PA1 also validated the remarkable mechanical response. In the initial loading stage, instead of showing tensile strain concentration at a single location and developing a localized crack, smeared strain showed up at the tensioned region of the PA1 specimen.

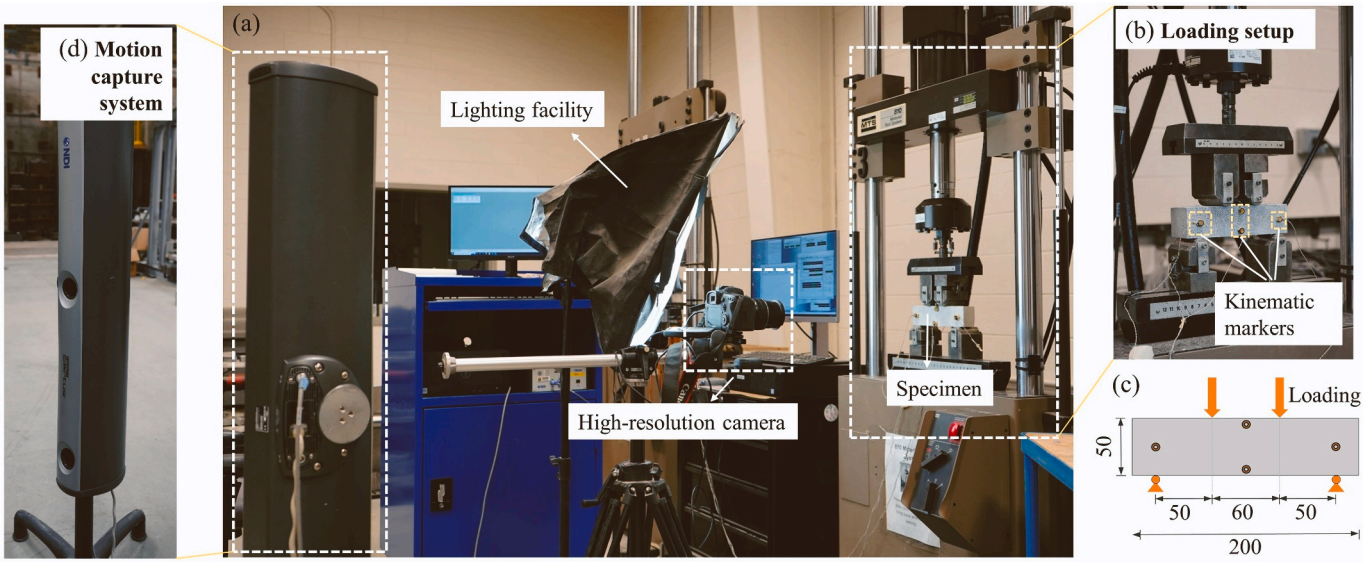

Fig. 9. Test setups.

In Fig. 10b, the DIC-analyzed image illustrates the distribution of horizontal tensile strain (ε_{xx}). It should be noted that the subscript of ε_{xx} stands for the horizontal direction in the analyzed image, not the printing direction of 3DP. Smeared tensile strain (the red regions) indicates multiple cracking sites. As confirmed in the bottom view image, dense micro-cracks were captured.

The flexural performance of PA1 remarkably outperformed that of cast ECC, with higher flexural strength and more ductile response. Moreover, the PA1 group also showed a substantially different failure mode from cast ECC. PA1 group generated denser micro-cracks in the tension region, and the main fracture crack was tortuous along the height of the specimens (Fig. 10b); in contrast, cast ECC showed fewer cracks on the bottom and bunches of straight cracks on the front (Fig. 10e). There are three primary sources of these differences:

(1) Fiber alignment in 3DP-ECC. It has been reported in 3D extrusion that the fibers tend to align along the printing direction, i.e., the direction of nozzle movement [37]. It is the same case for 3DP-ECC in this research. As shown in Fig. 11, the PVA fibers exhibited a strong orientation tendency along the x-direction in the filaments. Compared to cast ECC with random fiber distribution, consistency in fiber orientation resulted in a more robust tensile and flexural resistance, inducing denser micro-cracks in the tension region (see Fig. 10b and e). This made PA1 a more favorable orientation, as fibers exhibited the best crack bridging capacity in the x-direction.

(2) Crack bifurcation and deflection in a laminate structure. The stacked parallel ECC filaments resemble the layered structure of laminate composites and therefore share a similar crack propagation pattern. In four-point bending tests, the tension region at the bottom layer/filaments was subjected to the highest tensile strain and therefore was the location where cracks initiated. After the load-bearing capacity of the bottom filaments was exhausted, the cracks penetrated through the layer and were deflected into the interface/interlaminar region, creating an interface delamination crack. As can be appreciated in Fig. 12a, after the crack ① penetrated the lowermost layer, the crack tip developed in two different directions along the interface, crack ② and ③. Nonetheless, deflected cracks did not persist along the interface. Since the maximum bending stress in the experiment was located at the mid-span and decreased along the span, the driving force for the interfacial crack propagation gradually reduced [65]. Under the loading circumstance, the ratio of driving forces (energy release rate) and resistance (crack extension resistance or fracture roughness) of the crack tip could vary in two directions, that is, along the interface or into the adjacent layer. When the ratio in the latter scenario surpasses the former, the crack tip tends to kink out into the upper layer/filament [66]. This crack bifurcation depends on the local driving forces and local material characteristics (R) of both the interface and the filament matrix near the interfacial area. In Fig. 12a, crack ③ was kinked into crack site ⑤ after advancing for approximately 12 mm (Fig. 12b), and the main crack continued to develop along the interface for another 10 mm and then kinked into crack site ⑥ (Fig. 12a and c).

The deflection and bifurcation processes occurred successively during the test, as shown in Fig. 12a. For example, after crack ④ cut through the filament, the crack was further deflected to a horizontal crack ⑦ (Fig. 12a and d). Repeated crack deflections were also captured in the front view of Fig. 10b. The spacing between each reorientation of crack was approximately the layer thickness, confirming that the distortion of cracks occurred at the interlayer position. Furthermore, a zigzag fracture crack was observed on the bottom view in Fig. 10b, illustrating that the crack kinking occurred not only on the x-z plane and at interlayer interfaces, but in the interior of the specimen and at the inter-filament interfaces. Both crack deflection and bifurcation promote energy dissipation and reduce the overall rate of crack development, thereby enhancing the damage tolerance of the printed parallel ECC filaments.

(3) Crack trapping feature of ECC. As kinked out from the interface, the crack tip experiences a low initial toughness in the matrix and attempts to keep growing into the upper filament. In the case of brittle bulk material, the filament would be penetrated through and fractured at the cracking site. Conversely, if the bulk material has a rising fracture resistance, i.e., exhibits an R-curve characteristic [66], the resistance that the kinked crack tip encounters rapidly catches up with the driving force due to fiber bridging, then the advance of the crack can be stopped. In this case, the kinked cracks are trapped in the filament. Cracks ⑤ and ⑥ in Fig. 12a evidenced the crack kinking-trapping mechanism in 3DP-ECC. Both cracks were kinked out from the interfacial crack

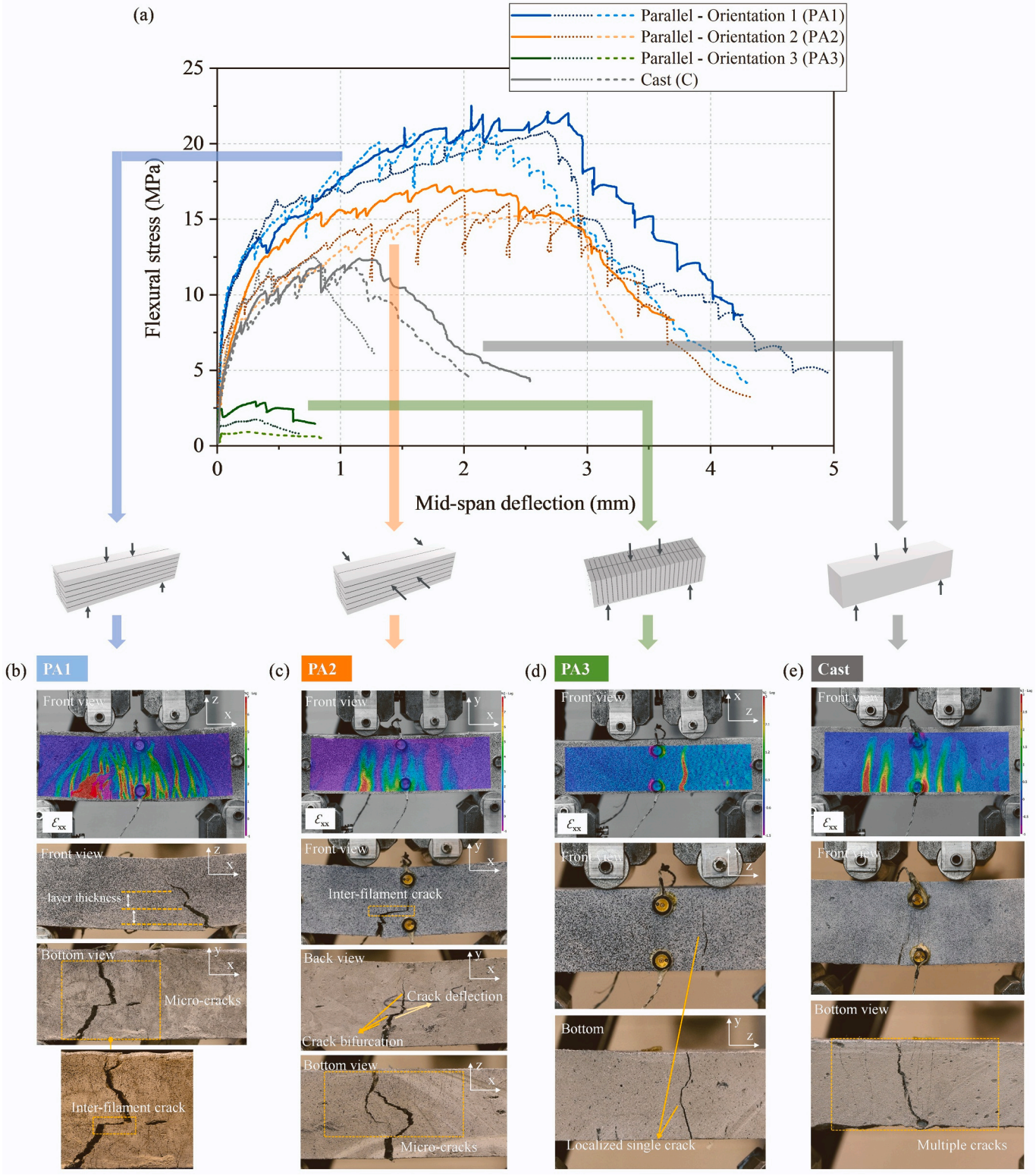

Fig. 10. Flexural performance of parallel ECC filaments and cast ECC in four-point bending tests.

③ to the filament matrix, showing concentrated tensile strain at the cracking sites in Fig. 12c, then trapped by fiber bridging inside the filament with no further propagation along either vertical or horizontal directions. The crack kinking-trapping mechanism of 3DP-ECC facilitates energy consumption and yields a more ductile mechanical response.

Under the synergistic effect of the above factors, the flexural performance of PA1 notably exceeded those of the other groups in Fig. 10a. In addition to the highest flexural strength, PA1 also exhibited remarkable energy absorption capacity. The area under the stress-deflection curve of the PA1 group is approximately 3–4 times that of the cast ECC. The excellent energy absorption capacity removes the dependence on steel reinforcement, enabling robust structural integrity

Fig. 11. Fiber alignment observed in 3DP-ECC.

and reliability through the combination of 3DP technology and ductile ECC materials.

Parallel filaments loaded in Orientation 2 (PA2) possessed a slightly lower flexural strength than PA1 while exhibited a similar failure mode. In the tensioned zone of the specimen, dense micro-cracks were developed (bottom view in Fig. 10c), as the fiber alignment still imparted a reliable crack bridging ability in the x-direction under the loading scenario of PA2. The relative reduction in flexural strength in PA2 was attributed to the slight difference in crack propagation modes. As illustrated before, cracks in PA1 were deflected at the interlayer positions, while in PA2, similar deflections occurred on the inter-filament surfaces (see the front view and back view in Fig. 10c). Due to the geometrical difference in filament width and height, PA2 contained fewer interfaces in the x-y plane, indicating less chance of crack deflection and bifurcation and impairing the energy dissipation capability. Nonetheless, extensive deflection and distortion of cracks were captured in the interior of the specimen due to the existence of layer interfaces in the x-z plane (bottom view in Fig. 10c). Although the overall flexural performance was slightly inferior to PA1, the mechanical response of PA2 was notably improved when compared to cast ECC, attributed to the influences of the three factors demonstrated above.

Despite the excellent flexural properties of parallel filaments in Orientation 1 and 2, the performance in Orientation 3 (PA3) showed a dramatic drop. Due to the fiber alignment along the x-direction, layer interfaces had insufficient fiber bridging and thus became the most vulnerable positions when parallel to the loading direction. Once a crack was initiated in the tensioned matrix, the lack of fiber bridging cannot stop the crack or bear a higher load during the crack propagation and eventually developed into a localized fracture crack. Consequently, different from the smeared multiple tensile cracks of PA1 and PA2, deformation localization into a single fracture was observed in the tension zone of PA3, as shown in the DIC-analyzed image in Fig. 10d. The interfacial failure inhibited the strain-hardening behavior of ECC material and induced drastic reductions, i.e., up to 91%, in strength and deflection compared with PA1. This is the primary concern about anisotropy in 3DP - the mechanical properties in Orientation 3 acutely deviate from the other two directions, raising doubts about the integrity and reliability of 3D printed structures in complex stress states and real application scenarios.

The impressive flexural performances of parallel filaments in Orientations 1 and 2 verified that 3D printing technology improved ECC performance at the structural scale through fiber alignment and laminate structural form. However, in Orientation 3, the emergence of anisotropy posed challenges to structural integrity. This apprehension gave rise to the attempts to mitigate anisotropy through the delicate design of innovative structural forms, i.e., knitted and tilted filaments, as depicted in the following subsections.

3.2. *Flexural properties of knitted filaments*

The four-point bending test results for knitted filaments and cast ECC specimens are summarized in Fig. 13a. Compared with parallel filaments, knitted filaments loaded in Orientation 1 (KN1) and Orientation 2 (KN2) showed inferior flexural strength and mid-span deflection. This is due to the fact that the parallel filaments aligned all fibers to the x-direction to the greatest extent, maximizing the performance in PA1 and

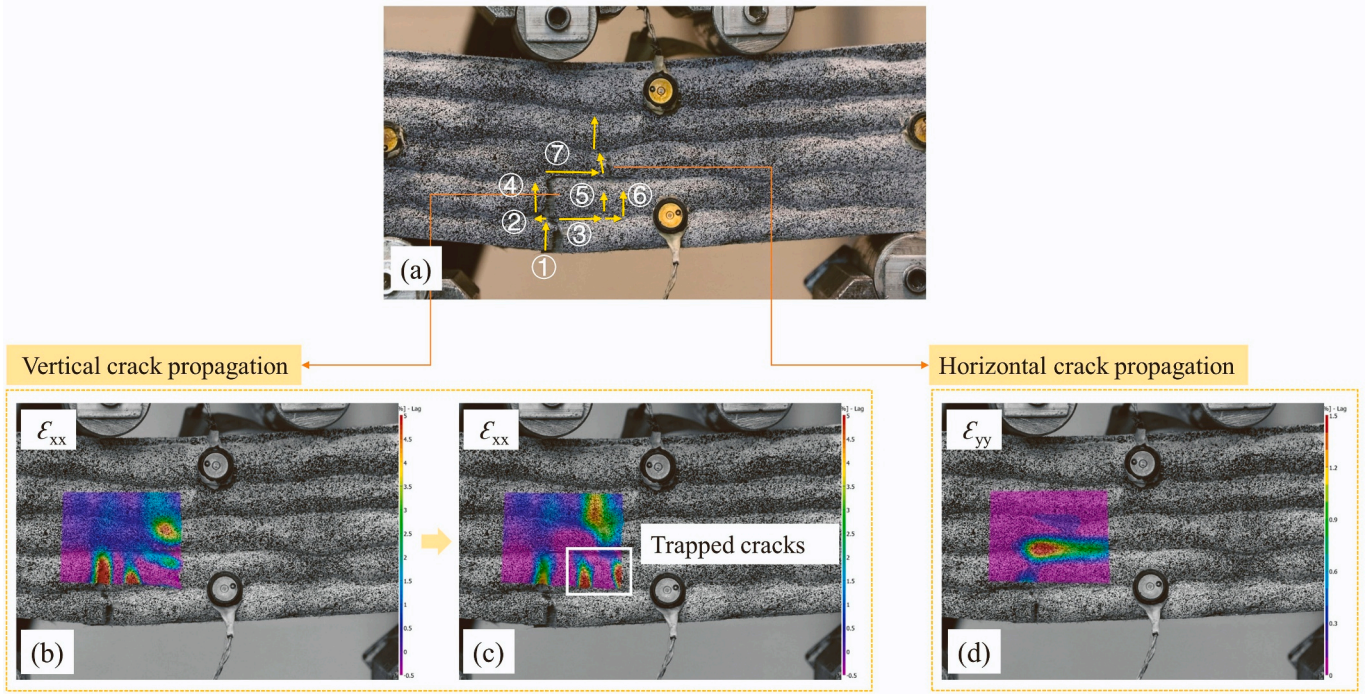

Fig. 12. Crack kinking and trapping in 3DP-ECC. (The arrows indicate the propagating directions of visible cracks.)

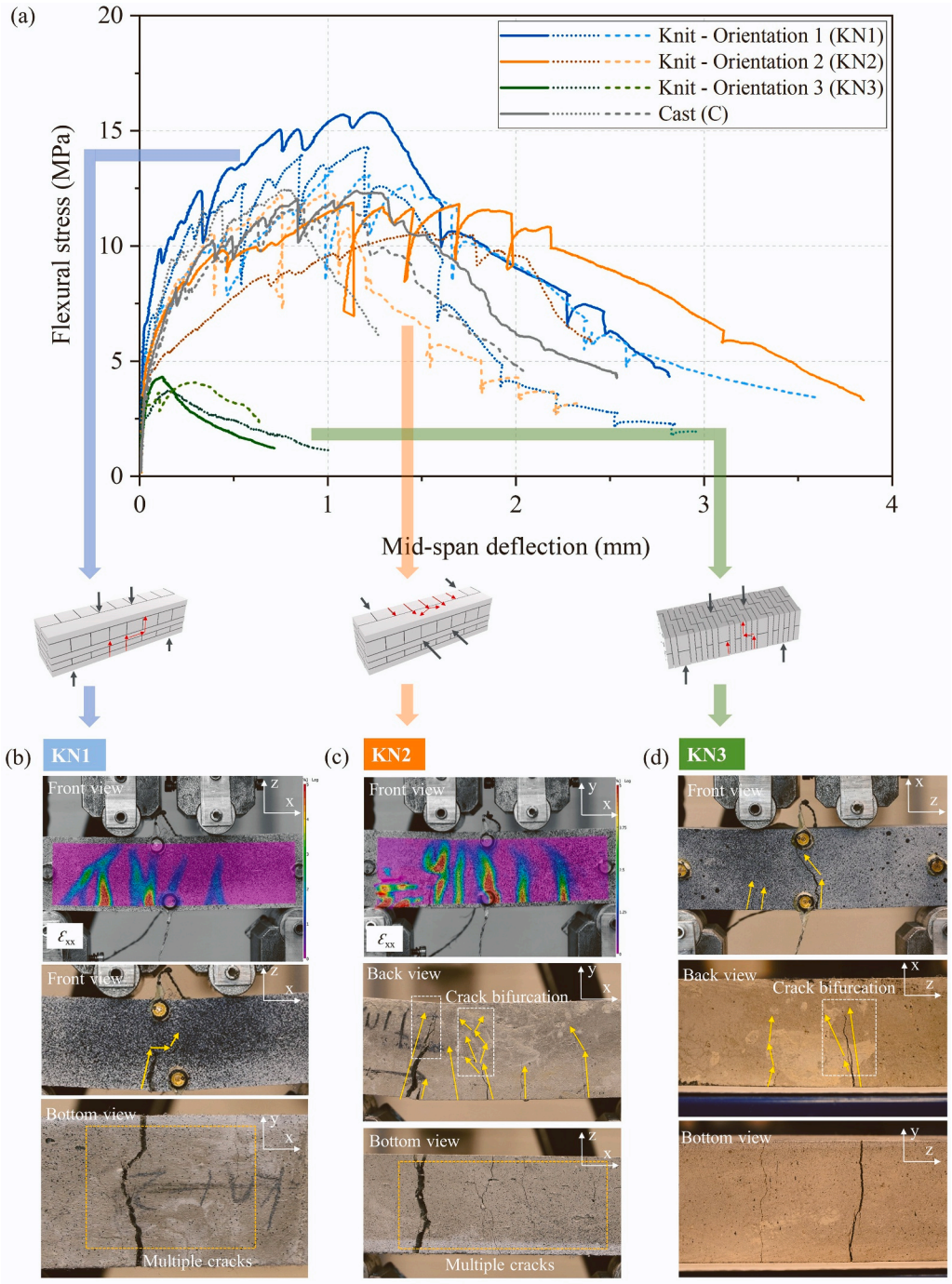

Fig. 13. Flexural performance of knitted ECC filaments in four-point bending tests. (The red arrows in the schematic diagrams indicate the potential cracking sites; the yellow arrows in (b-d) represent the propagating directions of visible cracks.) (For interpretation of the references to colour in this figure legend, the reader is referred to the web version of this article.)

PA2 loading cases. However, unlike parallel printing, knitting altered the orientation of some filaments in the architected structure, diverting part of the fiber alignment from the x-direction to other directions. Due to the presence of filaments deposited along the y- and z-directions, the proportion of fibers arranged along the x-direction was reduced, thus impairing the flexural properties of KN1 and KN2. Despite the weakened performance, KN1 outperformed its cast counterpart in flexural properties, while KN2 exhibited comparable performance with cast ECC. Therefore, knitted filaments loaded in Orientation 1 and 2 were able to meet the requirements of the same application scenarios as cast ECC.

Knitting created a different failure pattern than cast ECC and parallel filaments. Generally, in the four-point bending tests, tensile cracks were initiated at multiple locations on the bottom of all PA1, PA2, KN1, and KN2 specimens. In the PA1 group, cracking arose in the bulk material of the continuous filaments, whose properties were homogenous along the x-direction. The cracks thereby had a uniform probability to develop at random positions along the entire tension zone, thus forming dense cracks that were closely spaced. In KN1, however, there was a priority in the crack initiation location. As seen in the bottom view in Fig. 13b, spacing between main cracks was approximately 30 mm, i.e., the width of a single filament, verifying that cracks tended to develop at the inter-filament interfaces between adjacent y-direction filaments. This

tendency restrained the initial crack development, limited the energy-releasing rate, and weakened the overall ductility compared with the parallel filaments.

The bottom cracks progressed along interfaces in the loading direction. Further deflection and bifurcation occurred when they were deflected into the x-direction filament. This phenomenon was more pronounced in KN2. As shown in Fig. 13c, the bottom cracks fully developed along the inter-filament interfaces and advanced for some distance in the y-direction. When reaching the intersection of filaments, the cracks entered the continuous x-direction filament. Cracks experienced successive bifurcations and extended toward surrounding areas. A dendritic cracking pattern was thus shaped. Deflection and bifurcation of cracks, as previously elucidated, promoted energy dissipation and delayed failure to achieve excellent ductility in PA2. The ultimate fracture surface (Fig. 14) also confirmed that the deliberate design of a complex interface system promotes a more tortuous fracture path of the printed ECC structure. Since the width of the filament was three times the height, x-direction filaments accounted for a larger proportion in the x-y plane than in the x-z plane, as shown in the cracking schematic diagrams. Thus, KN2 was generally more conducive to crack bifurcation within the filament, yielding greater mid-span deflections and superior ductility.

In Orientation 3 (KN3), improved flexural properties over parallel filaments (PA3) were presented. Regarding the cracking mode, bottom cracks had the same tendency to initiate at the interlayer interfaces. However, the number of cracks developed was not as numerous as in KN1 and KN2 (Fig. 13d). During the upward progression, one main crack was deflected into a diagonal direction when encountering the inter-layer interface (front view in Fig. 13d). While in the back view, the orientation of the same crack was less inclined, indicating there was crack distortion inside the specimen. Furthermore, bifurcated cracks were captured in the back view and bottom view. Overall, no significant enhancement in mid-span deflection was seen in KN3, compared to PA3. However, non-singular cracks and crack deflection and bifurcation contributed significantly to strength. Up to 116% increase in flexural strength in Orientation 3 was observed when the knitting pattern was applied.

In general, knitting filaments created a unique flexural failure mode and allowed for deliberate performance tuning of 3DP-ECC. The flexural strengths of knitted filaments in Orientation 1 and 2 were inferior to those of parallel filaments; however, the rich cracking patterns coupled with the filament's tensile resistance induced comparable or even superior performance to cast ECC. It was observed in both KN1 and KN2 that cracks commonly started at the inter-filament positions and then were interrupted by the continuous filaments midway. Cracks were forced to zigzag into the interior of the filament and bifurcated successively, forming more crack tips and a more complex crack network. During this process, the strain-hardening behavior of the specimen was guaranteed, and fracture failure was delayed.

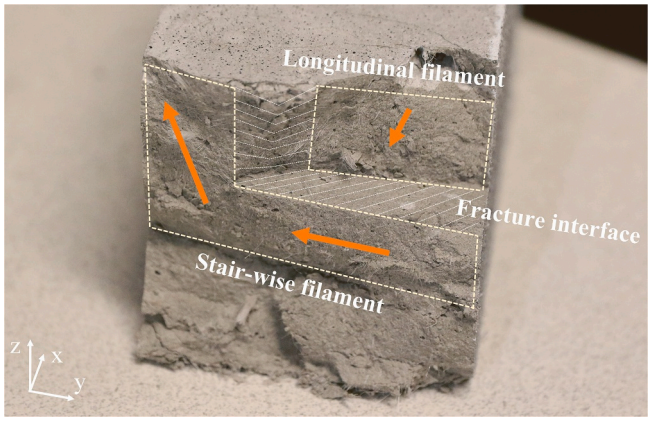

Fig. 14. Fracture surface of knitted ECC loaded to complete fracture.

3.3. Flexural properties of tilted filaments

The four-point bending test results for tilted filaments and cast ECC specimens are summarized in Fig. 15a. The flexural strengths of tilted filaments in Orientation 1 and 2 fell between those of parallel filaments and knitted filaments, while still remained prominently higher than the cast counterparts.

Regarding the fracture mode, it was found that the crack patterns of TI1 and TI2 were analogous to those of KN1 and KN2. Multiple tensile cracks arose from the tension zone at the bottom of the specimen. Since both short filament segments (parallel to the y-z plane) and continuous longitudinal filaments (along the x-direction) were included in the bottom region, deflection and branching were observed at the bottom cracks (bottom views in Fig. 15b and c). As the cracks progressed upward along the loading direction, deflection was observed at the intersection of the interfaces with different orientations. Cracks were prone to branching after being kinked into longitudinal filaments, resulting in an expanded crack distribution (front and back views in Fig. 15b and c).

Compared with KN1 and KN2, the interface system of tilted filament was relatively plain, including inclined inter-layer and inter-filament ones orthogonal to each other. This means it may be easier for a crack to penetrate and cause damage through the flat interface than through a complex zig-zag interface. As a result, despite the higher flexural strength, TI1 and TI2 possessed relatively lower mid-span deflections than knitted filaments. The ductility of TI1 was comparable to that of cast ECC, while the mid-span deflection of TI2 specimens was slightly weakened.

In Orientation 3 (TI3), a remarkable superiority of tilted filaments was demonstrated - TI3 showed a drastic boost in flexural strength compared to PA3. As seen in the bottom view of Fig. 15d, the tensile cracks started approximately along the direction of the inclined layer interface. However, unlike PA3, which split rapidly from a simple straight crack, TI3 experienced crack deflection and bifurcation. This indicated that the crack advancing inside the specimen did not completely follow the flat layer interface. Instead, twisting and turning of cracks in the interior took place. In addition, the crack was deflected from the layer interface into the inter-filament one in the middle of the upward progress and turned diagonally into a filament. Corresponding to this crack deflection was a slight stress drop on the stress-deflection curve, followed by a re-uplift, which symbolized the redistribution of stress and the increase in bearing capacity due to interior fiber bridging. Consequently, the peak stress of TI3 reached 279% of PA3. A stress-softening segment was observed thereafter, with progressive crack opening and failure of fiber bridging.

Generally, the failure modes of tilted filaments were similar to those of knitted filaments, benefiting from crack deflection and bifurcation. Furthermore, substantial increases in flexural strength compared to knitted filaments and cast ECC were witnessed. The main contributing factor is the designed interface system. Nonetheless, the ductility of TI1 and TI2 were comparable to or slightly weaker than that of cast ECC.

3.4. Discussion on flexural properties and anisotropy

The flexural strengths and mid-span deflections of the three printing patterns and cast ECC are presented in Fig. 16. In Orientation 1 and 2, the flexural strength of most printed specimens surpassed their cast counterparts, except for KN2 which possessed a slightly lower strength than the reference. The most favorable PA1 was observed with an average flexural strength of 21.6 MPa, revealing a 73% increase compared to cast ECC. For PA2, the increase percentage was 35%. In addition, KN1 and TI1 also achieved 118% and 142% of the cast strength. Regarding mid-span deflection, PA1 and PA2 exceeded the cast equivalent by 155% and 93%, respectively. For KN1 and KN2, this increase was 20% and 45%. Tilted filaments showed comparable

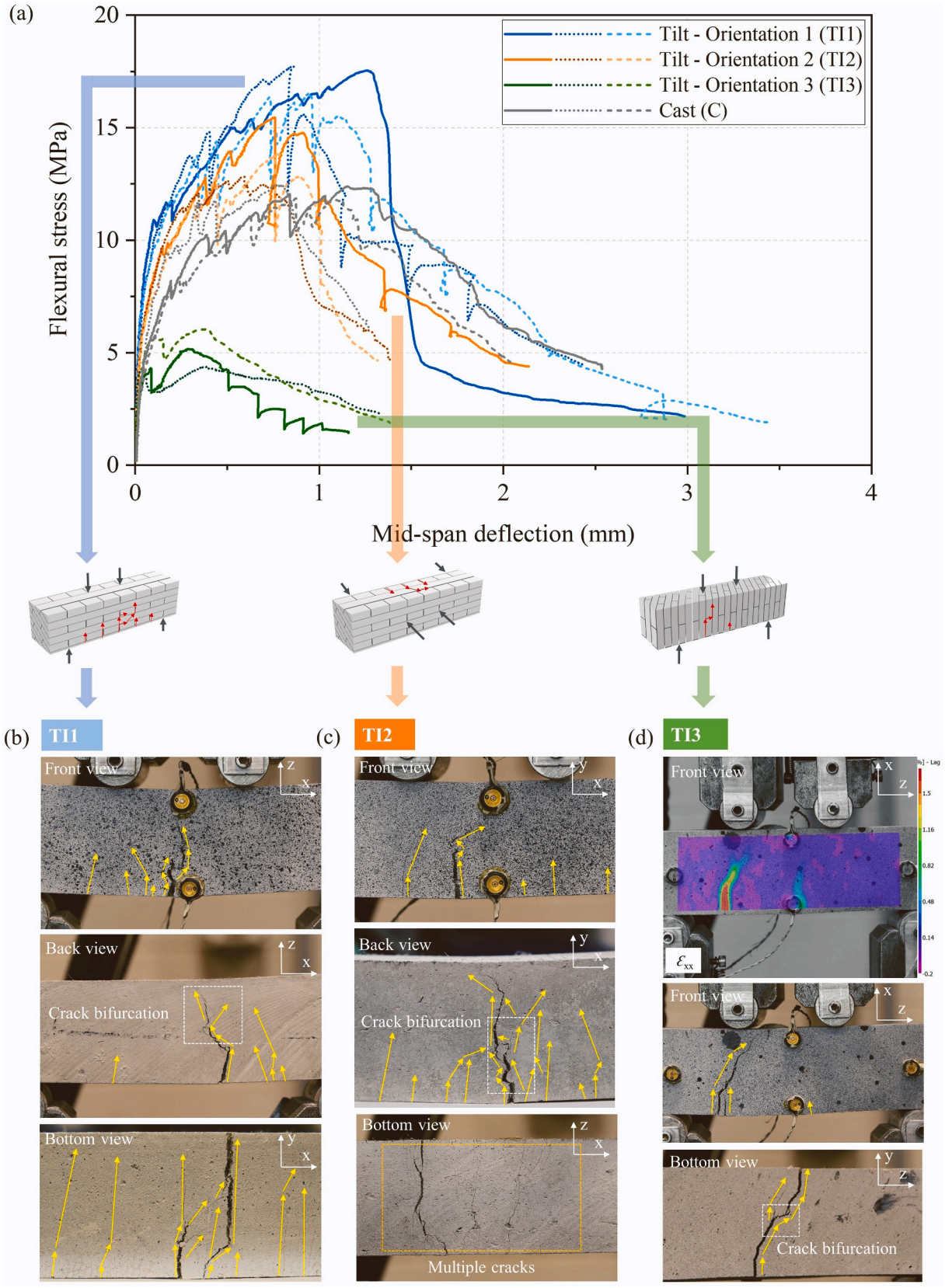

Fig. 15. Flexural performance of tilted ECC filaments in four-point bending tests. (The red arrows in the schematic diagrams indicate the potential cracking sites; the yellow arrows in (b-d) represent the propagating directions of visible cracks.) (For interpretation of the references to colour in this figure legend, the reader is referred to the web version of this article.)

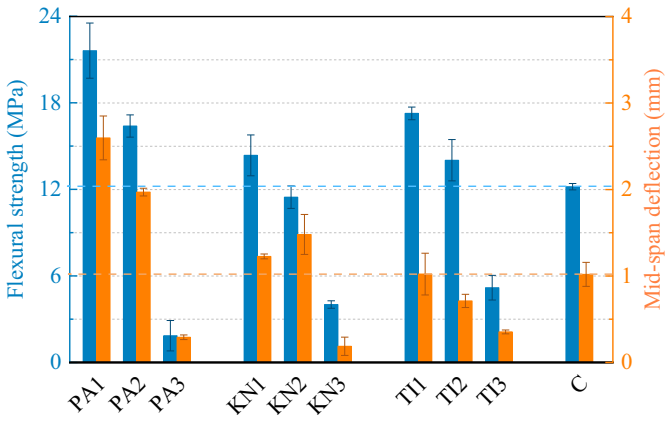

Fig. 16. Flexural strengths and mid-span deflections of printed and cast ECC.

deflection to cast ECC in Orientation 1, while amounted to 70% of cast ECC in Orientation 2. Additionally, in Orientation 1 and 2, knitted and tilted filaments established their respective advantages in strength and ductility. The difference in path design made knitted filaments more ductile, while tilting filaments resulted in higher bearing capacity. In general, the flexural performance of various 3DP-ECCs in Orientation 1 and 2 had transcended or at least was comparable to the integral cast ECC. This means that under those two load scenarios, 3DP-ECC can meet the same structural requirements as cast ECC and provide more reliable capacity.

In Orientation 3, remarkable enhancements of flexural strength were obtained by knitting and tilting filaments. An up-to-179% increase was observed in TI3, and the strength of KN3 also exceeded that of PA3 by 116%. It is worth noting that, despite the high strength of KN3, the corresponding deflection was reduced compared to PA3, and a strain-softening behavior was captured. For TI3, nonetheless, the increases in strength and deflection occurred simultaneously. As illustrated in the previous subsection, the flexural stress elevated again after the stress drop caused by initial cracking, delaying the overall failure of the specimens.

The preeminent strength of printed ECC compared to cast one can be attributed to the fiber alignment and the kinking-trapping mechanism of ECC. The former renders filaments with the maximum tensile resistance in the printing direction. In the cases of knitted and tilted structures, the fiber bridging capacity is further allocated to different orientations, as shown in Fig. 17. While the latter takes advantage of the interfaces and ECC's material features to capture and trap cracks during their progression, thereby effectively enhancing the mechanical response of the structure.

Regarding anisotropy, the ratios of the strengths in Orientation 2 (f_2) and Orientation 3 (f_3) relative to Orientation 1 (f_1) are presented in Fig. 18. For all three different printing patterns, f_2/f_1 values are approximately 0.8, showing that strength difference in these two directions is not the primary concern regarding anisotropy. Knitting and tilting slightly improve the ratio with a limited margin. For f_3/f_1, however, there is a notable improvement with knitting and tilting. In this research, f_3 is merely 8.6% of f_1 in conventional parallel printing, causing concerning anisotropy. While in the case of knitted and tilted filaments, the f_3/f_1 ratio is promoted to 28% and 30%, respectively, demonstrating an effective alleviation of anisotropy. This improvement originates from the architectured structural forms with tortuous interfaces.

It is worth noting that the mechanical properties of the printed structures are also substantially affected by multiple factors, e.g., printing setups, material compositions, structural geometry, printing parameters, etc. Therefore, the effect of knitting and tilting filaments on mitigating anisotropy is not limited to increasing the f_3/f_1 ratio to 30%. In an optimized printing scenario, the reference value of f_3/f_1 in parallel

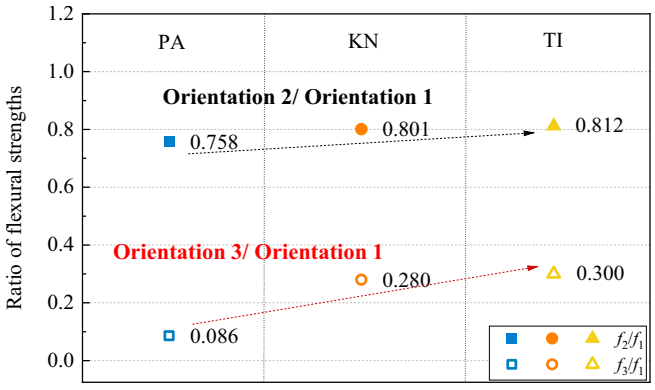

Fig. 18. Ratios of flexural strengths in different loading orientations.

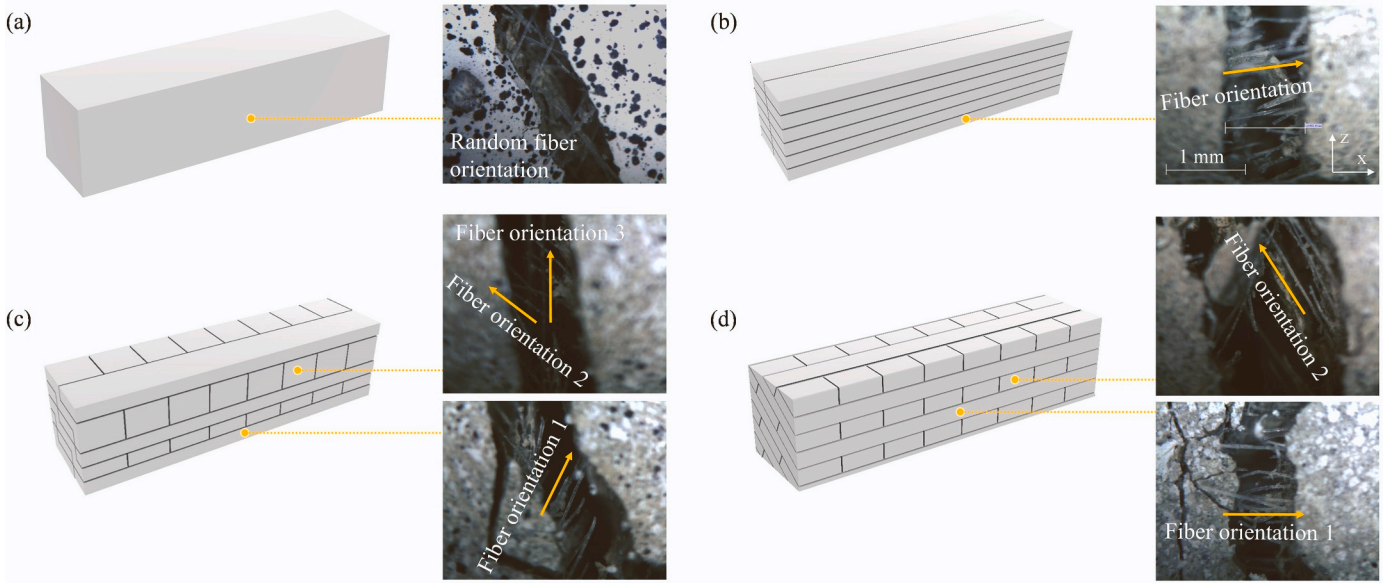

Fig. 17. Microscopic illustration of fiber alignment in (a) cast ECC, (b) parallel filaments, (c) knitted filaments, and (d) tilted filaments.

filaments can exceed the ratio in this study, and the effectiveness of knitting and tilting will be further improved to achieve better homogenization of the 3DP-ECC structure.

3.5. Challenges and limitations

The innovative approach presented in this study represents a novel direction for addressing the anisotropy concern in 3DP-ECC. Nevertheless, it is essential to acknowledge the limitations in both research and practical applications to further enhance existing methodologies and guide future investigations in this area. Several challenges and limitations are identified below:

(1) Anisotropy alleviation has been confirmed with the proposed innovative printing patterns. However, more improvements can be made to further address the anisotropy issue. Given the excellent mechanical performance of 3DP-ECC in Orientation 1 and 2, there is still a gap between Orientation 3 and the other two in terms of strength and ductility. From the perspective of fracture mode, the designed patterns have the potential to induce more tensile cracks under Orientation 3 loading. The pattern design should be further refined and optimized to obtain more desirable cracking modes and stimulate higher structural bearing capacity and ductility.
(2) The proposed printing method may pose a minor influence on printing efficiency. As the number of individual tool paths is increased compared with parallel patterns, the total transition time, i.e., the time gap for the tool to move from the ending point of the previous paths to the starting point of the following paths, is elongated. Nonetheless, this influence is insignificant based on experimental experience, as the automated construction is not interrupted, and the printing tool runs continuously throughout the printing process. Furthermore, this concern could be addressed through path design, e.g., connecting two adjacent layers at an "end-and-start" location.
(3) Without steel reinforcement used in 3DP-ECC, durability concerns associated with steel corrosion are diminished. Nonetheless, considering the complex interfaces introduced by the proposed printing method, further research should be conducted to probe the ingression and transportation mechanism of chemical agents inside 3DP-ECC and the degradation of fibers and matrix in harsh environments.

4. Conclusions

The present study developed two innovative printing patterns, knitted and tilted filaments, for 3DP-ECC. Both filaments were printed and saw-cut for four-point bending tests. In addition, conventional parallel filaments and cast ECC were used as references. Through experimental investigation and analysis, the following conclusions can be drawn:

(1) Knitted and tilted filaments were designed to mimic the crossed-lamellar micro-structure of conch shells. The three-dimensional space design rendered ECC's directional-dependent tensile/flexural resistance to the element out of the conventional printing plane (x-y plane). Moreover, the patterns introduced a more complex three-dimensional interface system, which converted the original structural weakness into a structural strengthening method.
(2) In four-point bending tests, parallel filaments loaded in Orientation 1 and 2 showed excellent flexural properties and robust strain-hardening behavior, notably outperforming the cast counterparts. The advancement was attributed to three primary sources: ① fiber alignment in extruded ECC filaments; ② crack bifurcation and deflection in the laminate structure; and ③ crack trapping feature of ECC.
(3) Due to the unitary orientation of interfaces and lack of fiber bridging, the flexural performance of parallel filaments in Orientation 3 showed a dramatic drop compared with the other two orientations. The interfacial single-crack failure inhibited the strain-hardening behavior of ECC material and induced drastic reductions, i.e., up to 91%, in flexural strength. The emergence of anisotropy poses great challenges to structural integrity.
(4) Knitted and tilted filaments showed superior or comparable bending performance to cast ECC in Orientations 1 and 2. Furthermore, knitting and tilting filaments created a unique flexural failure mode and allowed for deliberate performance tuning of 3DP-ECC. In four-point bending tests, multiple tensile cracks arose from the tensioned zone at the bottom and progressed in the loading direction. Further deflection and bifurcation occurred when the cracks encountered filament intersections, promoting sufficient energy dissipation and delaying failure to achieve desirable ductility.
(5) Effective mitigation in anisotropy was captured, which can be attributed to the improved fracture resistance in the weakest orientation achieved through innovative printing patterns. In Orientation 3, remarkable enhancements of flexural strength were obtained by knitting and tilting filaments, compared to parallel filaments. An up-to-179% increase was observed in tilted filaments, and the strength of knitted filaments also exceeded that of parallel filaments by 116%. The ratio of the strength in Orientation 3 (f_3) relative to Orientation 1 (f_1) was increased from 8.6% to 30%, indicating remarkable alleviation of anisotropy in 3DP-ECC. This improvement primarily originates from the architected structural forms with tortuous interfaces in knitted and tilted filaments.

The strength of this method in alleviating anisotropy lies in that no external reinforcements are necessary, and the automated construction process is not interrupted. 3DP technology's flexibility in enabling more design freedoms is maximally exploited, and ECC's excellent material features are taken advantage of. Furthermore, by building complex interface systems, the proposed patterns convert interfaces from vulnerable weak links in a structure into an effective means to strengthen the printed structure and delay failure. With the feasibility of these alleviation methods verified, more effective and efficient structural forms can be created following this inherent logic in future research.

CRediT authorship contribution statement

Wen Zhou: Conceptualization, Methodology, Investigation, Validation, Writing – original draft. **Wes McGee:** Conceptualization, Methodology, Investigation, Writing – review & editing. **H. Süleyman Gökçe:** Investigation. **Victor C. Li:** Conceptualization, Methodology, Supervision, Writing – review & editing.

Declaration of Competing Interest

The authors declare that they have no known competing financial interests or personal relationships that could have appeared to influence the work reported in this paper.

Data availability

Data will be made available on request.

Acknowledgments

Financial support for this research is provided by the University of

Michigan MCubed 3 Program, the Center for Low Carbon Built Environment (CLCBE) and the James R. Rice Distinguished University Professorship. The Department of Civil and Environmental Engineering at the University of Michigan provides financial support for the robotic 3DP equipment. W. Zhou is supported by a University of Michigan fellowship for graduate studies. H. Süleyman Gökçe would like to acknowledge the postdoctoral research fellowship supported by The Scientific and Technological Research Council of Türkiye (TÜBİTAK).

References

[1] G. Ma, R. Buswell, W.R. Leal Da Silva, L. Wang, J. Xu, S.Z. Jones, Technology readiness: a global snapshot of 3D concrete printing and the frontiers for development, Cem. Concr. Res. 156 (2022) 106774, https://doi.org/10.1016/j.cemconres.2022.106774.

[2] R.A. Buswell, W.R. Leal De Silva, S.Z. Jones, J. Dirrenberger, 3D printing using concrete extrusion: a roadmap for research, Cem. Concr. Res. 112 (2018) 37–49, https://doi.org/10.1016/j.cemconres.2018.05.006.

[3] I. Agustí-Juan, G. Habert, Environmental design guidelines for digital fabrication, J. Clean. Prod. 142 (2017) 2780–2791, https://doi.org/10.1016/j.jclepro.2016.10.190.

[4] I. Agustí-Juan, F. Müller, N. Hack, T. Wangler, G. Habert, Potential benefits of digital fabrication for complex structures: environmental assessment of a robotically fabricated concrete wall, J. Clean. Prod. 154 (2017) 330–340, https://doi.org/10.1016/j.jclepro.2017.04.002.

[5] G. De Schutter, K. Lesage, V. Mechtcherine, V.N. Nerella, G. Habert, I. Agusti-Juan, Vision of 3D printing with concrete — technical, economic and environmental potentials, Cem. Concr. Res. 112 (2018) 25–36, https://doi.org/10.1016/j.cemconres.2018.06.001.

[6] M.K. Mohan, A.V. Rahul, G. De Schutter, K. Van Tittelboom, Extrusion-based concrete 3D printing from a material perspective: a state-of-the-art review, Cem. Concr. Compos. 115 (2021) 103855, https://doi.org/10.1016/j.cemconcomp.2020.103855.

[7] R. Zhang, L. Wang, X. Xue, G. Ma, Environmental profile of 3D concrete printing technology in desert areas via life cycle assessment, J. Clean. Prod. 396 (2023) 136412, https://doi.org/10.1016/j.jclepro.2023.136412.

[8] F.P. Bos, C. Menna, M. Pradena, E. Kreiger, W.R.L. Da Silva, A.U. Rehman, D. Weger, R.J.M. Wolfs, Y. Zhang, L. Ferrara, V. Mechtcherine, The realities of additively manufactured concrete structures in practice, Cem. Concr. Res. 156 (2022) 106746, https://doi.org/10.1016/j.cemconres.2022.106746.

[9] C. Menna, J. Mata-Falcón, F.P. Bos, G. Vantyghem, L. Ferrara, D. Asprone, T. Salet, W. Kaufmann, Opportunities and challenges for structural engineering of digitally fabricated concrete, Cem. Concr. Res. 133 (2020) 106079, https://doi.org/10.1016/j.cemconres.2020.106079.

[10] M. Bazli, H. Ashrafi, A. Rajabipour, C. Kutay, 3D printing for remote housing: benefits and challenges, Autom. Constr. 148 (2023) 104772, https://doi.org/10.1016/j.autcon.2023.104772.

[11] W. Xu, S. Huang, D. Han, Z. Zhang, Y. Gao, P. Feng, D. Zhang, Toward automated construction: the design-to-printing workflow for a robotic in-situ 3D printed house, Case Stud. Construct. Mater. 17 (2022), e01442, https://doi.org/10.1016/j.cscm.2022.e01442.

[12] Z. Ahmed, R. Wolfs, F. Bos, T. Salet, A framework for large-scale structural applications of 3D printed concrete: the case of a 29 m bridge in the Netherlands, Open Conference Proc. 1 (2022) 5–19, https://doi.org/10.52825/ocp.v1i.74.

[13] F. Raaijmakers, Nijmegen has the longest 3D-printed concrete bicycle bridge in the world. https://www.tue.nl/en/news-and-events/news-overview/01-01-1970-nijmegen-has-the-longest-3d-printed-concrete-bicycle-bridge-in-the-world, 2021.

[14] S. Bhooshan, V. Bhooshan, A. Dell Endice, J. Chu, P. Singer, J. Megens, T. Van Mele, P. Block, The striatus bridge, Architect. Struct. Construct. 2 (2022) 521–543, https://doi.org/10.1007/s44150-022-00051-y.

[15] Zaha Hadid Architects, Striatus 3D Printed Concrete Bridge. https://www.zaha-hadid.com/design/striatus, 2021.

[16] Vertico, Concrete Printed Shell Pavilion Revealed. https://www.vertico.xyz/hpa, 2022.

[17] T. Ding, J. Xiao, V. Mechtcherine, Microstructure and mechanical properties of interlayer regions in extrusion-based 3D printed concrete: a critical review, Cem. Concr. Compos. 141 (2023) 105154, https://doi.org/10.1016/j.cemconcomp.2023.105154.

[18] T.T. Le, S.A. Austin, S. Lim, R.A. Buswell, R. Law, A.G.F. Gibb, T. Thorpe, Hardened properties of high-performance printing concrete, Cem. Concr. Res. 42 (2012) 558–566, https://doi.org/10.1016/j.cemconres.2011.12.003.

[19] B. Zareiyan, B. Khoshnevis, Effects of interlocking on interlayer adhesion and strength of structures in 3D printing of concrete, Autom. Constr. 83 (2017) 212–221, https://doi.org/10.1016/j.autcon.2017.08.019.

[20] N. Roussel, F. Cussigh, Distinct-layer casting of SCC: the mechanical consequences of thixotropy, Cem. Concr. Res. 38 (2008) 624–632, https://doi.org/10.1016/j.cemconres.2007.09.023.

[21] B. Panda, N.A. Noor Mohamed, S.C. Paul, G. Bhagath Singh, M.J. Tan, B. Šavija, The effect of material fresh properties and process parameters on buildability and interlayer adhesion of 3D printed concrete, Materials 12 (2019) 2149, https://doi.org/10.3390/ma12132149.

[22] B. Panda, S.C. Paul, N.A.N. Mohamed, Y.W.D. Tay, M.J. Tan, Measurement of tensile bond strength of 3D printed geopolymer mortar, Measurement 113 (2018) 108–116, https://doi.org/10.1016/j.measurement.2017.08.051.

[23] E. Keita, H. Bessaies-Bey, W. Zuo, P. Belin, N. Roussel, Weak bond strength between successive layers in extrusion-based additive manufacturing: measurement and physical origin, Cem. Concr. Res. 123 (2019) 105787, https://doi.org/10.1016/j.cemconres.2019.105787.

[24] J.G. Sanjayan, B. Nematollahi, M. Xia, T. Marchment, Effect of surface moisture on inter-layer strength of 3D printed concrete, Constr. Build. Mater. 172 (2018) 468–475, https://doi.org/10.1016/j.conbuildmat.2018.03.232.

[25] J. Van Der Putten, M. Deprez, V. Cnudde, G. De Schutter, K. Van Tittelboom, Microstructural characterization of 3D printed cementitious materials, Materials 12 (2019) 2993, https://doi.org/10.3390/ma12182993.

[26] G. Ma, Z. Li, L. Wang, F. Wang, J. Sanjayan, Mechanical anisotropy of aligned fiber reinforced composite for extrusion-based 3D printing, Constr. Build. Mater. 202 (2019) 770–783, https://doi.org/10.1016/j.conbuildmat.2019.01.008.

[27] T. Wangler, N. Roussel, F.P. Bos, T.A.M. Salet, R.J. Flatt, Digital concrete: a review, Cem. Concr. Res. 123 (2019) 105780, https://doi.org/10.1016/j.cemconres.2019.105780.

[28] T. Ding, J. Xiao, S. Zou, Y. Wang, Hardened properties of layered 3D printed concrete with recycled sand, Cem. Concr. Compos. 113 (2020) 103724, https://doi.org/10.1016/j.cemconcomp.2020.103724.

[29] Y. Yang, C. Wu, Z. Liu, H. Wang, Q. Ren, Mechanical anisotropy of ultra-high performance fibre-reinforced concrete for 3D printing, Cem. Concr. Compos. 125 (2022) 104310, https://doi.org/10.1016/j.cemconcomp.2021.104310.

[30] R.J.M. Wolfs, F.P. Bos, T.A.M. Salet, Hardened properties of 3D printed concrete: the influence of process parameters on interlayer adhesion, Cem. Concr. Res. 119 (2019) 132–140, https://doi.org/10.1016/j.cemconres.2019.02.017.

[31] B. Panda, S.C. Paul, M.J. Tan, Anisotropic mechanical performance of 3D printed fiber reinforced sustainable construction material, Mater. Lett. 209 (2017) 146–149, https://doi.org/10.1016/j.matlet.2017.07.123.

[32] B. Nematollahi, M. Xia, P. Vijay, J.G. Sanjayan. Chapter 18 - Properties of Extrusion-Based 3D Printable Geopolymers for Digital Construction Applications, 3D Concrete Printing Technology, Butterworth-Heinemann, 2019, pp. 371–388. 10.1016/B978-0-12-815481-6.00018-X.

[33] B. Zhu, J. Pan, B. Nematollahi, Z. Zhou, Y. Zhang, J. Sanjayan, Development of 3D printable engineered cementitious composites with ultra-high tensile ductility for digital construction, Mater Design 181 (2019) 108088, https://doi.org/10.1016/j.matdes.2019.108088.

[34] T. Ding, J. Xiao, S. Zou, X. Zhou, Anisotropic behavior in bending of 3D printed concrete reinforced with fibers, Compos. Struct. 254 (2020) 112808, https://doi.org/10.1016/j.compstruct.2020.112808.

[35] H. Ogura, V. Nerella, V. Mechtcherine, Developing and testing of strain-hardening cement-based composites (SHCC) in the context of 3D-printing, Materials 11 (2018) 1375, https://doi.org/10.3390/ma11081375.

[36] S.C. Figueiredo, C.R. Rodríguez, Z.Y. Ahmed, D.H. Bos, Y. Xu, T.M. Salet, O. Çopuroğlu, E. Schlangen, F.P. Bos, An approach to develop printable strain hardening cementitious composites, Mater Design 169 (2019) 107651, https://doi.org/10.1016/j.matdes.2019.107651.

[37] S.C. Figueiredo, C.R. Rodríguez, Z.Y. Ahmed, D.H. Bos, Y. Xu, T.M. Salet, O.G. Ç. Glu, E. Schlangen, F.P. Bos, Mechanical behavior of printed strain hardening cementitious composites, Materials 13 (2020) 2253, https://doi.org/10.3390/ma13102253.

[38] M. Hambach, D. Volkmer, Properties of 3D-printed fiber-reinforced Portland cement paste, Cem. Concr. Compos. 79 (2017) 62–70, https://doi.org/10.1016/j.cemconcomp.2017.02.001.

[39] F.P. Bos, E. Bosco, T.A.M. Salet, Ductility of 3D printed concrete reinforced with short straight steel fibers, Virtual Phys. Prototyping 14 (2018) 160–174, https://doi.org/10.1080/17452759.2018.1548069.

[40] K. Yu, W. McGee, T.Y. Ng, H. Zhu, V.C. Li, 3D-printable engineered cementitious composites (3DP-ECC): fresh and hardened properties, Cem. Concr. Res. 143 (2021) 106388, https://doi.org/10.1016/j.cemconres.2021.106388.

[41] N. Xu, Y. Qian, J. Yu, C.K.Y. Leung, Tensile performance of 3D-printed strain-hardening cementitious composites (SHCC) considering material parameters, nozzle size and printing pattern, Cem. Concr. Compos. 132 (2022) 104601, https://doi.org/10.1016/j.cemconcomp.2022.104601.

[42] X. Sun, J. Zhou, Q. Wang, J. Shi, H. Wang, PVA fibre reinforced high-strength cementitious composite for 3D printing: mechanical properties and durability, Additive Manufact 49 (2022) 102500, https://doi.org/10.1016/j.addma.2021.102500.

[43] T. Marchment, J. Sanjayan, M. Xia, Method of enhancing interlayer bond strength in construction scale 3D printing with mortar by effective bond area amplification, Mater Design 169 (2019) 107684, https://doi.org/10.1016/j.matdes.2019.107684.

[44] E. Hosseini, M. Zakertabrizi, A.H. Korayem, G. Xu, A novel method to enhance the interlayer bonding of 3D printing concrete: an experimental and computational investigation, Cem. Concr. Compos. 99 (2019) 112–119, https://doi.org/10.1016/j.cemconcomp.2019.03.008.

[45] G. Ma, N.M. Salman, L. Wang, F. Wang, A novel additive mortar leveraging internal curing for enhancing interlayer bonding of cementitious composite for 3D printing, Constr. Build. Mater. 244 (2020) 118305, https://doi.org/10.1016/j.conbuildmat.2020.118305.

[46] V.C. Li, F.P. Bos, K. Yu, W. McGee, T.Y. Ng, S.C. Figueiredo, K. Nefs, V. Mechtcherine, V.N. Nerella, J. Pan, G.P.A.G. van Zijl, P.J. Kruger, On the emergence of 3D printable engineered, strain hardening cementitious composites

(ECC/SHCC), Cem. Concr. Res. 132 (2020) 106038, https://doi.org/10.1016/j.cemconres.2020.106038.
[47] J.V.D. Putten, G.D. Schutter, K.V. Tittelboom, Surface modification as a technique to improve inter-layer bonding strength in 3D printed cementitious materials, RILEM Tech. Lett. 4 (2019) 33–38, https://doi.org/10.21809/rilemtechlett.2019.84.
[48] T. Marchment, J. Sanjayan, Mesh reinforcing method for 3D concrete printing, Automat. Constr. 109 (2020) 102992, https://doi.org/10.1016/j.autcon.2019.102992.
[49] T. Marchment, J. Sanjayan, in: Penetration reinforcing method for 3D concrete printing, Second RILEM International Conference on Concrete and Digital Fabrication, Springer International Publishing, Cham, 2020, pp. 680–690. https://doi.org/10.1007/978-3-030-49916-7_68.
[50] J. Kruger, A. Cicione, F. Bester, M. van den Heever, S. Cho, R. Walls, G. van Zijl, in: Facilitating ductile failure of 3D printed concrete elements in fire, Second RILEM International Conference on Concrete and Digital Fabrication, Springer International Publishing, Cham, 2020, pp. 449–458. https://doi.org/10.1007/978-3-030-49916-7_46.
[51] O. Geneidy, S. Kumarji, A. Dubor, A. Sollazzo, in: Simultaneous reinforcement of concrete while 3D printing, Second RILEM International Conference on Concrete and Digital Fabrication, Springer International Publishing, Cham, 2020, pp. 895–905. https://doi.org/10.1007/978-3-030-49916-7_87.
[52] L. Wang, G. Ma, T. Liu, R. Buswell, Z. Li, Interlayer reinforcement of 3D printed concrete by the in-process deposition of U-nails, Cem. Concr. Res. 148 (2021) 106535, https://doi.org/10.1016/j.cemconres.2021.106535.
[53] V. Nguyen-Van, S. Li, J. Liu, K. Nguyen, P. Tran, Modelling of 3D concrete printing process: a perspective on material and structural simulations, Addit. Manufac. 61 (2023) 103333, https://doi.org/10.1016/j.addma.2022.103333.
[54] L.T. Kuhn-Spearing, H. Kessler, E. Chateau, R. Ballarini, A.H. Heuer, S.M. Spearing, Fracture mechanisms of the Strombus gigas conch shell: implications for the design of brittle laminates, J. Mater. Sci. 31 (1996) 6583–6594, https://doi.org/10.1007/BF00356266.
[55] S. Kamat, X. Su, R. Ballarini, A.H. Heuer, Structural basis for the fracture toughness of the shell of the conch Strombus gigas, Nature 405 (2000) 1036–1040, https://doi.org/10.1038/35016535.
[56] H. Zhu, K. Yu, W. McGee, T.Y. Ng, V.C. Li, Limestone calcined clay cement for three-dimensional- printed engineered cementitious composites, ACI Mater. J. 118 (2021) 111–222, https://doi.org/10.14359/51733109.
[57] A.L. van Overmeir, S.C. Figueiredo, B. Šavija, F.P. Bos, E. Schlangen, Design and analyses of printable strain hardening cementitious composites with optimized particle size distribution, Constr. Build. Mater. 324 (2022) 126411, https://doi.org/10.1016/j.conbuildmat.2022.126411.
[58] V.C. Li. Engineered Cementitious Composites (ECC), 1st ed., Springer, Berlin, Germany, 2019, 978-3-662-58437-8, https://doi.org/10.1007/978-3-662-58438-5.
[59] B. Nematollahi, P. Vijay, J. Sanjayan, A. Nazari, M. Xia, V. Naidu Nerella, V. Mechtcherine, Effect of polypropylene fibre addition on properties of Geopolymers made by 3D printing for digital construction, Materials 11 (2018) 2352, https://doi.org/10.3390/ma11122352.
[61] B. Zhu, J. Pan, Z. Zhou, J. Cai, Mechanical properties of engineered cementitious composites beams fabricated by extrusion-based 3D printing, Eng. Struct. 238 (2021) 112201, https://doi.org/10.1016/j.engstruct.2021.112201.
[62] J. Ye, C. Cui, J. Yu, K. Yu, J. Xiao, Fresh and anisotropic-mechanical properties of 3D printable ultra-high ductile concrete with crumb rubber, Compos. Part B 211 (2021) 108639, https://doi.org/10.1016/j.compositesb.2021.108639.
[63] T. Ding, J. Xiao, S. Zou, J. Yu, Flexural properties of 3D printed fibre-reinforced concrete with recycled sand, Constr. Build. Mater. 288 (2021) 123077, https://doi.org/10.1016/j.conbuildmat.2021.123077.
[64] F. Aslani, R. Dale, F. Hamidi, A. Valizadeh, Mechanical and shrinkage performance of 3D-printed rubberised engineered cementitious composites, Constr. Build. Mater. 339 (2022) 127665, https://doi.org/10.1016/j.conbuildmat.2022.127665.
[65] P.M. Pohl, F. Kümmel, C. Schunk, I. Serrano-Munoz, H. Markötter, M. Göken, H. W. Höppel, About the role of interfaces on the fatigue crack propagation in laminated metallic composites, Materials (Basel) 14 (2021) 2564, https://doi.org/10.3390/ma14102564.
[66] Y.M. Lim, V.C. Li, Durable repair of aged infrastructures using trapping mechanism of engineered cementitious composites, Cem. Concr. Compos. 19 (1997) 373–385, https://doi.org/10.1016/S0958-9465(97)00026-7.